https://doi.org/10.1016/j.seppur.2018.05.033

Microfiber-nanofiber composite filter for high-efficiency and low pressure drop under nano-aerosol loading

Wallace Woon-Fong Leung*, Curie Wing-Yi Hau, Hung-Faat Choy

Mechanical Engineering

The Hong Kong Polytechnic University

Here

Hung Hom, Hong Kong

*Corresponding author, Email: mmwleung@polyu.edu.hk

Abstract

Nano-aerosols are airborne aerosols in the range of 100nm. They are present abundantly in both pollutants and viruses, both of which affect human health. Filtering these nano-aerosols leads to high-pressure drop in cabin filters due to their small sizes forming impermeable dust cake, and prior to cake formation the capture efficiency is rather poor with conventional microfiber filters.

We have investigated a composite filter with a microfiber layer positioned immediately upstream of a nanofiber layer. Such composite filter provides high efficiency and low-pressure drop during all phases of filtration of nano-aerosols: initial depth filtration, transition, and final cake filtration. The behavior of the composite filter together with various filter benchmarks (single and composite filters of microfiber/nanofiber filters) has been investigated by monitoring the pressure drop, especially during cake filtration. Using the measurements together with Ergun/Kozeny-Carman equation and material balance we come up with a new method to determine the solid volume fraction and permeability of the cake. The grade efficiency for the most penetrating particle is also measured concurrently to define the incipient point to cake formation and provide material balance.

Most importantly, for the first time we have confirmed that the cake ultimately forms on the composite filter is due to the cake that originates from the upstream microfiber layer and not from the downstream nanofiber layer. Therefore, the pressure drop for the composite filter can be sustained relatively low throughout the filtration. On the other hand, the aerosol capture efficiency stays very high from start-to-end of filtration, with high initial filtration efficiency courtesy of the nanofiber filter installed downstream of the composite filter. The price to pay is a slight higher pressure drop for the composite filter in the clean unloaded state, but this is insignificant during aerosol loading as most pressure drop is attributed to the cake.

For the first time we have introduced, also independently using Buckingham-Pi analysis, a brand new dimensionless parameter, Beta, which measures the equivalent "thickness" of additional cake deposition (in molten form) to the viscous flow resistance "distance" due to the additional cake deposit. A high-capacity filter aimed for heavy aerosol loading should have large Beta that results in low solidosity, high porosity, and high permeability for the cake. In our study, the microfiber-nanofiber composite filter has the highest Beta of nearly 4 and also highest efficiency. Despite high efficiency the single nanofiber filter has much lower Beta of 2, while the single microfiber filter has Beta of 3, yet much lower efficiency, especially at initial filtration. Using the microfiber-nanofiber composite filter design, we can "engineer the cake" deposited on the filter to be more permeable and with least flow resistance during aerosol loading to attain high Beta values. This is an innovative approach to increase the badly needed aerosol storage capacity with low pressure drop for the filter while maintaining high efficiency throughout the aerosol loading for extended filtration applications. The highly permeable aerosol cake can also be cleaned by backpulsed-and-backblow readily for filter reuse.

Keywords:

Composite microfiber-nanofiber filter; nano-aerosols; aerosol loading; cake; air filtration; Beta

1. Introduction

1.1 Nano-aerosols

Nano-aerosols are airborne aerosols with size 100nm and below. Given their small sizes, they can be inhaled in large amount into our bodies and can diffuse readily from the lung to the circulation system causing various chronic cardiovascular diseases. These nano-aerosols can be pollutants emitted from diesel vehicles or even gasoline vehicles. The particle size is typically 10-100nm before agglomeration from collision. Photochemical smog, which results from photo-oxidation with presence of nitrogen oxides and hydrocarbon gases in presence of sunlight, can also generate these fine aerosols. When these aerosols agglomerate to a certain size, say 400-700nm, they reflect sunlight and become visible as smog or haze. On the other hand, air-borne viruses such as common cold, influenza A, as well as other air-borne viruses (e.g. bird flu, swine flu, SARS, MERS, etc.) are also about 50-100nm before attaching to a nucleus particle during air-borne. Measurements of these aerosols, in particular 100nm, in office and outdoor environment can reach 60-300 million count/m^3 (unpublished measurement from the authors), which is quite alarming! Cabin filter used in confined spaces, such as trains, planes, and vehicles are in great demand. People get sick frequently after having been confined in the plane, train, and vehicle, especially for long-distance ride. This can pose as an impending societal issue for which solutions are badly needed.

1.2 Curtailing pressure drop maintaining high capture efficiency under aerosols loading

Filters made of microfibers are not effective in capturing mechanically (by diffusion and interception) the nano-aerosols [1]. HEPA filter can be used to remove the nano-aerosols yet the pressure drop is significantly high. On the other hand, electret microfiber made from charged polypropylene [2-4] can boost the filtration efficiency but once the fibers are covered with aerosol deposit, their electrostatic interaction with the aerosols is lost. On the other hand, filter made of electrospun nanofibers [5-7] can be used to capture these nano-aerosols effectively [1]. The efficiency for capture depends on the amount, measured in grams per square meter (gsm), of nanofibers used. Usually much lower amount of nanofibers is used as compared with microfiber filters due to nanofibers are more effective in filtration and it is desirable to avoid incurring high pressure drop associated with nanofibers. For a fixed amount of nanofibers targeting at a given filtration efficiency, the pressure drop of the filter can be reduced by splitting the same total amount of nanofibers into multiple layers (i.e. multi-layering), or stack-up arrangement, instead of placing all the fibers in a single layer [1, 8].

Recently, research efforts are focused in developing nanofiber composite that include aerogels [9], carbon nanotubes [10], nanofiber with microfiber mixed [11] and various stack-up nanocomposite geometries [12, 13]. All these efforts concentrate on the material and design of the filter, and performance evaluation are strictly on a clean filter without aerosol loading. These are not applicable for applications for extended filter use, such as for cabin filter in vehicles and airplanes, HVAC, space filtration in auditorium and hospital wards, clean room, engine, turbine, air intake, and industrial filtrations.

On the other hand, under aerosol loading the filtration can change from depth filtration, transition and cake filtration [14, 15, 16]. In depth filtration, aerosols are trapped mechanically by diffusion and

interception in the filter [1]. The aerosols are not uniformly captured across the filter thickness and there is more aerosol deposit near the upstream end of the filter facing the air flow [17]. This is because the captured aerosols in the upstream filter become sites for capturing more incoming aerosols producing an avalanche effect. This region is “the skin layer” with most of the aerosol deposition. It also accounts for majority of the pressure drop across the filter due to flow blockage by the trapped aerosols. Eventually, the deposited aerosols not only plug up the flowable channels in the skin layer of the filter but further builds up above the filter surface in form of dendritic bridges. As these dendrite/bridge structures further interact with each other, a cake layer is formed continuously on the filter surface. As more aerosols are deposited, a relatively homogeneous cake layer forms on the filter surface. The incoming aerosols are completely captured by the cake, which serves as the effective filter medium. As the cake thickens, most of the pressure drop occurs across the cake layer and not across the partially clogged filter media [14].

It is imperative to “engineer” the cake of a filter to have a porous, permeable structure incurring low-pressure drop while capturing all incoming aerosols. To-date, this is an important missing gap that has seldom been addressed. Microfiber filter has a rather low capture efficiency for nano-aerosols; however, the pressure drop during both depth filtration and cake filtration is relatively low. In depth filtration mode, given the filtration is less effective the deposit onto the large microfibers in the filter is modest and the deposit do not clog up the flowable passages. The pressure drop is therefore relatively low. As cake forms on the surface of the filter through the skin effect as with the nanofiber filter, the cake is quite porous and permeable. The air flow resistance is also low. The only disadvantage of microfiber filter is that prior to cake forming on the microfiber filter surface, the capture efficiency on nano-aerosols is rather low. Therefore, it is reasonable to have a nanofiber filter being installed immediately downstream of the microfiber filter forming a composite filter [18, 19] to raise the efficiency to an acceptable level. However, for such composite filter a cake can still form as more aerosol deposit on the

downstream nanofiber filter. With more aerosol deposition, the cake from the nanofiber layer grows inside the microfiber layer. The cake deposit gets “rearranged” or “loosened” by the microfibers as well as its aerosols deposit, which can take form of individual aerosols, aerosol dendrites, or dendritic bridges [14]. An outstanding issue is that would the cake from the nanofiber layer in the composite filter be more porous and permeable as compared to the cake without the microfiber filter layer positioned upstream (i.e. single nanofiber filter)? Another issue to be confirmed is that if the microfiber layer of the composite filter forms a cake on its own prior to the cake from the nanofiber growing from below, then the cake from the composite filter is almost the cake from the microfiber filter, which should be more porous and permeable. Which of these scenarios would happen in reality is quite intriguing? The cake growing from the nanofiber layer and being re-distributed or rearranged inside the microfiber in the composite filter (microfiber-nanofiber composite) should have resistance less than that from the single nanofiber filter alone. On the other hand, the cake growing out of the microfiber filter (outpacing that of the nanofiber filter downstream) in the composite filter should have flow resistance similar to that of the single microfiber filter alone. Therefore, with the objective of addressing the foregoing issues we will focus our investigation on the flow resistance during cake formation of the composite filter, and it will be benchmarked with other filters, especially single-layer nanofiber and microfiber filters, respectively.

1.3 Our study

In order to develop a filter that has low pressure drop and high efficiency throughout the aerosol loading, we investigate the cake deposition behavior of six filters, which are selected from nanofiber filter alone (two filters with different fiber diameters), microfiber filter alone, and a combination of micro-nanofiber filters in composite form and in separated form, and lastly nanofiber-nanofiber composite filter. These test filters are:

1. Nanofiber filter with 187nm fiber diameter.

2. Nanofiber filter with 283nm fiber diameter.
3. Microfiber filter with 2.7micon fiber diameter.
4. Microfiber (2.7micron) - nanofiber (187nm) composite filter.
5. Microfiber upstream and nanofiber separately located downstream (same filters as in 4.)
6. Nanofiber (283nm) - nanofiber (187nm) composite filter.

Under high aerosol loading condition, cake filtration predominates. We want to investigate the cake obtained from different filter configurations. In cake filtration, the pressure drop varies linearly with specific mass deposit and capture efficiency reaches 100%. We also link the incremental pressure drop per unit specific mass loading of the cake to the cake solid packing density (i.e. solidosity). When the solidosity is determined, the permeability of the cake can be determined from Darcy's law. Thus, cake permeability can be compared among different filter configurations.

2. Theoretical Consideration

The pressure drop Δp in the cake can be related by the Ergun equation to the face velocity over the cake V (=Q/A) where Q is the volumetric flow rate, A the filter area, d_p the equivalent mass mean diameter of the cake particles (assumed spherical), ΔL the cake thickness, μ the air viscosity, and ε_s the cake solidosity or cake solid volume fraction. If the particles are not spherical, a sphericity factor should be used. Thus,

$$\Delta p = \frac{150\mu}{d_p^2}\frac{\varepsilon_s^{\,2}}{(1-\varepsilon_s)^3}\Delta L V \qquad (1)$$

Note Eq. 1 is the Ergun equation for laminar flow as the inertial effect (i.e. quadratic term) is negligible due to Reynolds number being much less than unity. This form also coincides with the well-known Carman-Kozney equation except the constant being slightly different, 150 instead of 180. The slip factor is not taken into account as the count median diameter (CMD) of the particles in the experiments to be discussed in Section 3, 118nm, is twice the mean free path.

It is further assumed that the challenging aerosols are all fully captured by the cake and the cake thickness builds up over loading. Assuming the cake is not compactible (with internal rearrangement of particles over loading) and to a first approximation has constant solidosity ε_s, the mass of cake Δm being deposited on the filter surface is related to the cake thickness, ΔL, by material balance

$$\Delta m_s = \Delta m / A = \rho_s \varepsilon_s \Delta L \qquad (2)$$

Δm_s is the specific mass deposit, i.e. incremental mass deposited per unit filter area. From Eqs. 1 and 2, after ΔL is eliminated we obtain an equation for ε_s that depends on the slope $\Delta p/\Delta m_s$ in the cake filtration regime.

$$\varepsilon_s^3 - 3\varepsilon_s^2 + (3 + C)\varepsilon_s - 1 = 0 \qquad (3a)$$

$$C = \frac{150\mu V}{\rho_s d_p^2} \frac{1}{(\Delta p/\Delta m_s)} \qquad (3b)$$

The solution to the cubic equation, Eq. 3a, can be obtained readily using numerical algorithm, such as the Newton-Rapson method.

Given ε_s<<1, and O(ε_s^2) as well as higher orders can be neglected, an approximate solution to Eq. 3a is

$$\varepsilon_s \approx \frac{1}{3+C} \tag{4}$$

Darcy's law states that,

$$V = -\frac{K}{\mu}\frac{\Delta p}{\Delta L} \tag{5}$$

Comparing Eqs. 1 and 5, the permeability *K* becomes

$$K = \frac{d_p^2}{150}\frac{(1-\varepsilon_s)^3}{\varepsilon_s^{\,2}} \tag{6}$$

Therefore, the cake permeability *K* can be determined once the solidosity of the cake ε_s has been determined. From Eq. 6, it is observed that the smaller is ε_s, the higher is *K* at least to the first approximation.

3. Experiments

3.1 Aerosol generation and filter testing

There were two parts to the experimental set-up. The first part was the aerosol generation as shown in Fig. 1. Compressed air, after being filtered by a HEPA filter, was sent to an atomizer consisting of typically 0.1-2%w/w sodium chloride solution. When higher salt concentration was used, the system needed to be cleaned more frequently to avoid residual salt accumulated in the flow line that caused corrosion. The aerosol stream generated was sent to a membrane dryer where moisture was removed. The dried aerosol stream was then passed to an impactor where aerosols greater than 800nm were removed leaving undersize aerosols that were sent to a neutralizer for charging electrostatically. The charged aerosols were dispatched to a differential mobility analyzer, DMA, (not shown) that classified aerosol sizes by the charges deposited on these aerosols from the upstream ionizer. By tuning the DMA accordingly, a relatively monodispersed aerosol size was generated. After leaving the DMA, the aerosol

stream was sent to a second ionizer where the aerosols were neutralized. The aerosol stream was subsequently sent to the filter test column. The aerosol stream was further diluted with clean, filtered, make-up air. This resulting stream was used to challenge the "test filter" mounted in the test column as shown in Fig. 1. When measuring the grade efficiency, the DMA was tuned to deliver a given relatively monodispersed aerosol size, such as 300nm, to challenge the test filter. Upstream of the filter, a slip stream of the feed stream under isokinetic condition was being sent to the condensation particle counter (CPC) where the concentration of aerosols of known size was determined. The concentration of aerosols was also measured subsequently downstream of the filter. Based on the upstream and downstream concentration, C_u and C_d, respectively, the grade efficiency was determined. Thus,

$$\eta = 1 - \frac{C_d}{C_u} \qquad (7)$$

When the objective was to investigate the behavior of the test filter under aerosol loading, the DMA was deliberately bypassed leaving the polydispersed aerosol stream challenging the filter directly, otherwise, it took a long period to load up the filter with monodispersed aerosols and the test became impractically long. To further shorten the aerosol loading, a higher salt concentration was used to generate high aerosol concentration for accelerated loading. In addition, the pressure drop was continuously measured across the filter during the loading test as shown in Fig. 1.

While the pressure drop excursion over loading provided the loading behavior for the test filter, it was also useful to monitor the grade efficiency of the filter. It would be a serious disruption to measure the grade efficiency for all the aerosol sizes during the aerosol loading process, so only the most penetrating particle size (MPPS), taken here approximately as 300nm, was being monitored. When the efficiency of the MPPS reached closely to 100%, the filter would have undergone cake filtration or surface filtration and a linear trend in pressure drop was to be expected in subsequent loading. Based on the measured feed aerosol size distribution and its concentration for the specific size range, and face velocity of the

feed stream during loading, we can determine the total aerosols challenging the filter at any given time. In addition, from measurement of the filter efficiency, the amount of incoming aerosols being captured at any given time can be determined. By summing all the trapped aerosols by the test filter during the entire loading period, assuming no loss, the cumulative aerosols deposited on the filter can be determined.

A typical aerosol concentration versus size (40-500nm) is shown in Fig. 2. As can be seen, the maximum concentration exceeds $1x10^4$ /cm^3 at 105 nm. The CMD was 118.39nm while the mass mean diameter (MMD) was 331.71nm. At the two ends of the size spectrum, 40nm and 500nm, the aerosol count was much smaller, but their concentration number count still needed to exceed 100/cm^3 to maintain accuracy in determining the capture efficiency.

There were three different configurations for which the filters can be loaded with aerosols. These are shown by the schematics in Figs. 3(a) to 3(c). The arrow in the schematics represents the flow direction. Fig. 3a shows the standard configuration of testing one single filter (nanofiber filter or microfiber filter). Fig. 3b shows a microfiber filter being placed upstream of a nanofiber filter to assemble a composite filter. Fig. 3c shows a microfiber filter being placed upstream in a test column and the nanofiber filter is positioned separately far downstream in the test column. The results corresponding to all three filter configurations were compared at the end of the tests.

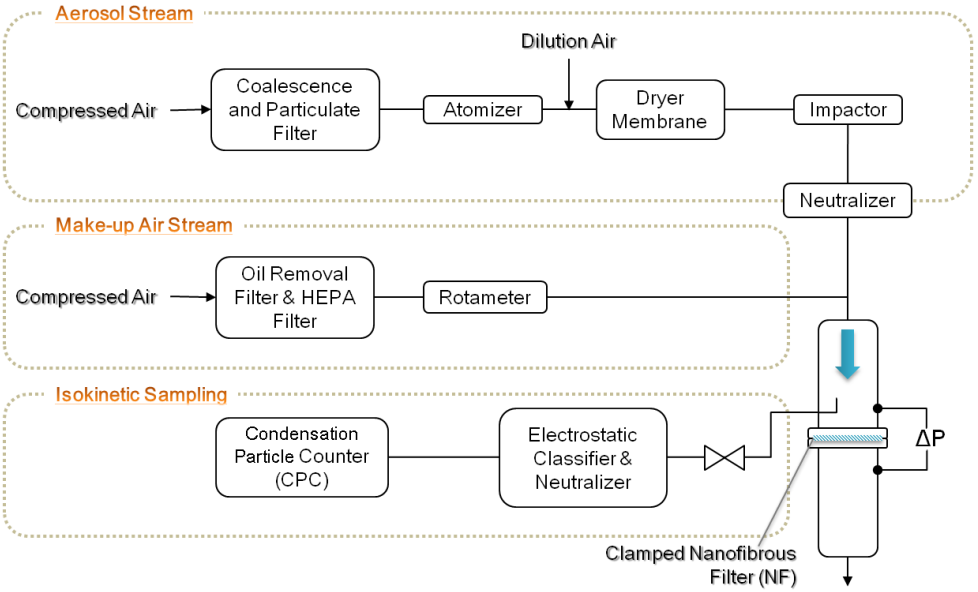

Fig. 1 – Aerosol generation and filter tester.

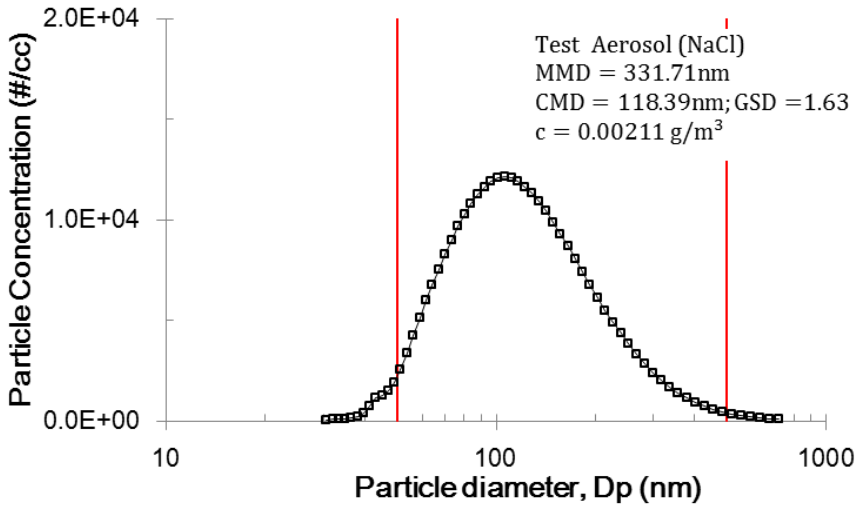

Fig. 2 – Aerosol concentration versus sizes generated for loading the test filter.

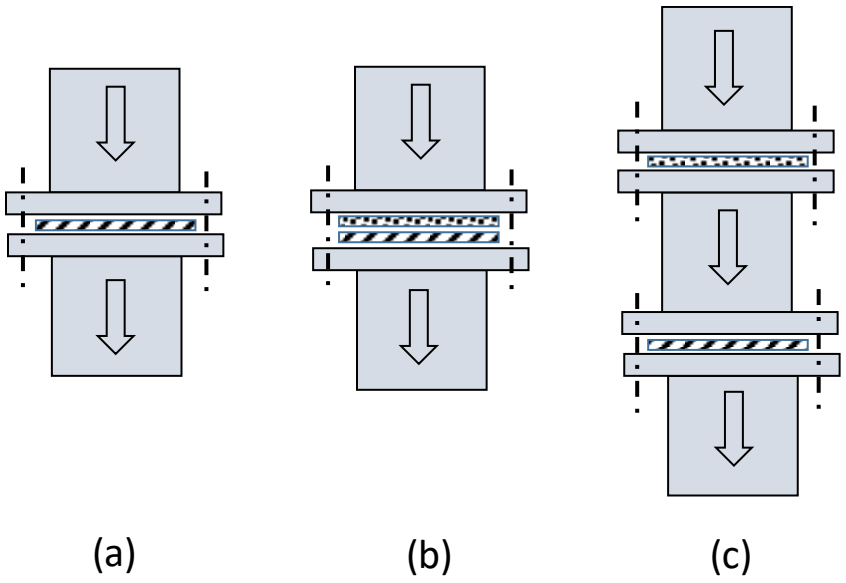

Fig. 3 – (a) Single test filter mounted in the test column, (b) a microfiber filter is positioned upstream of a nanofiber to form a composite filter, and (c) a microfiber filter is tested upstream in the test column far away from the nanofiber positioned downstream in the test column.

3.2 Test filters

The test filter was made in-house by electrospinning polyamide (Nylon 6, or abbreviated as N6) solution where N6 pellets were dissolved in formic acid. The precursor solution was well mixed and typical N6 concentration were 18-22%w/w. A nozzle-less electrospinning setup was used to produce nanofibers, see Fig. 4a. The precursor solution was brought by the rotating electrode to form a very thin sheet exposed in air. Under a high electrostatic field set up between the rotating electrode and the ground electrode, the electrostatic force became sufficiently high overcoming the surface tension of the thin

sheet. This resulted in a fiber jet being sent to the collector surface at the opposite ground electrode. During the free flight of the fiber jet, the repulsion force from neighboring positive charges deposited on the fiber repelled against each other, and together with evaporation of the formic acid solvent, the fiber thinned out to 100's of nanometers (i.e. nanofibers) before being collected at the far end ground electrode. Therefore, the controlling parameter were the voltage from feed to collector electrodes, typically 60kV to 80kV, distance of separation between feed to collector 0.15 to 0.19 m, and feed rate of the rotating electrode at 6 to 50 hz.

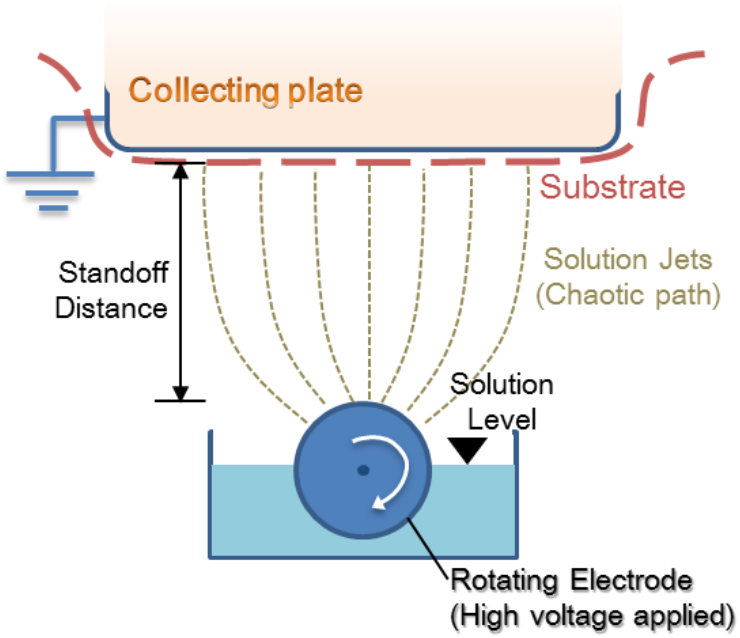

Fig. 4a – Schematic of needle-less electrospinning set-up.

Fig. 4b shows the fiber diameter as a function of concentration of N6 in solution. The fiber diameter was determined from the scanning electron microscope (SEM, JEOL Model JSM-6490, JEOL USA, Inc.). As can be seen in Fig. 4b, the fiber diameter increases rapidly as the precursor solution concentration is above

18%. The fiber diameter in our test filter ranged between 120nm to 283nm. The filter thickness of the produced nanofiber filter was typically 3 – 10 micrometers.

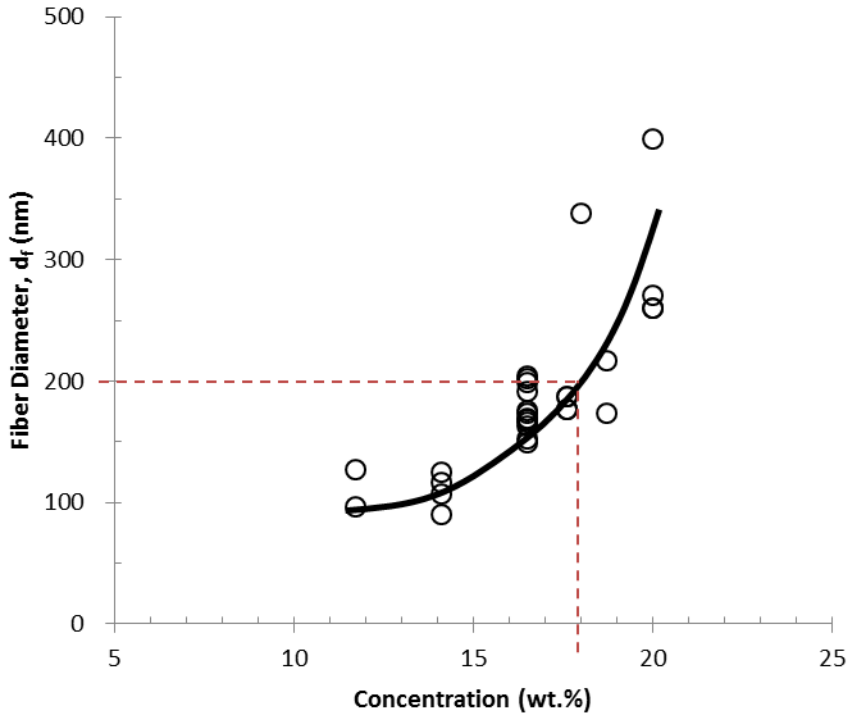

Fig. 4b – Fiber diameter as function of N6 in solution.

4. Results and discussion

4.1 Nanofiber filter (mean diameter 187nm)

The SEM image of the test filter with mean fiber diameter of 187nm is shown in Fig. 5a.

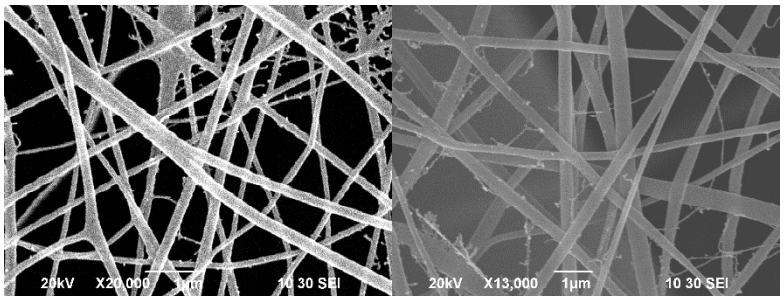

Fig 5a (left) – N6 test filter with average diameter 187nm, 5b (right) – N6 test filter with mean diameter 283nm.

Fig. 6 shows the loading curve for the 187nm nanofiber filter from aerosols with 40 to 500nm sodium chloride. The initial pressure drop for the clean filter prior to aerosol loading was 32.5Pa. The pressure drop Δp rose with increasing specific mass deposit, m/A, with a concave downward behavior until reaching a steady linear rate of increase. The latter was related to formation of cake above the nanofiber filter, which built up steadily over aerosol loading until the test ended with cumulative aerosol loading of m/A=20 gm^{-2}. The pressure drop across the filter and cake was registered at 850Pa. Initially, the cake captured only the coarser particles leaving the finer ones infiltrating through the cake and also the downstream nanofiber filter. (This is obtained by independent CFD to be presented elsewhere.) As aerosol loading continued with m/A between 3 and 5 gm^{-2}, even the finest particles below the 100nm got captured by the cake that became less permeable as these finer solids were captured in the finer pores of the cake structure. Therefore, the cake ultimately became an efficient filter media capturing challenging particles of all sizes between 40 and 500nm. Between 5 $gm^{-2} \leq m/A \leq 20$ gm^{-2} the aerosols were captured by the cake above the filter, while below 5 gm^{-2} the aerosols were mostly captured by depth filtration in the filter. This can be inferred based on the efficiency measurement of the 300nm aerosols shown on the same plot in Fig. 6. (If the 100nm aerosols were being monitored the result would not be far off from that of monitoring the 300nm aerosols.) Our results indicated that most captured aerosols (approximately 75%) for the total aerosol loading of 20 gm^{-2} was captured in the cake, and only 25% of the total aerosol was captured in the nanofiber filter. The large percentage of aerosols being captured in the cake is an atypical behavior under aerosol loading of nanofiber filter with low aerosol storage capacity in the filter.

The linear portion of the pressure excursion curve characterizes the cake filtration regime, the slope was determined to be 35.75(10^3) Pa-$kg^{-1}m^2$. By solving Eq. 3a using the Newton-Rapson method, the solidosity ε_s can be determined to be 0.0475 ($\varepsilon_s \approx 0.0472$ using the simplified Eq. 4) and the permeability K was subsequently determined from Eq. 6 to be 2.57(10^{-13})m^2. The cake solidosity ε_s, porosity ε (=1-ε_s), and permeability K are tabulated, respectively, in Table 1.

Table 1 – Properties of the cake for the nanofiber filter with fiber diameter d_f of 187nm

Δp_s (Pa)	32.5	ε_s (-)	0.0475
V (ms^{-1})	0.053	ε (-)	0.9525
ρ_s (kgm^{-3})	2200	K (m^2)	2.57(10^{-13})
$\Delta p/m$ (Pa-$kg^{-1}m^2$)	35.75(10^3)		
μ ($kgm^{-1}s^{-1}$)	1.81(10^{-5})		
d_p(m)	317(10^{-9})		
C (-)	18.21		

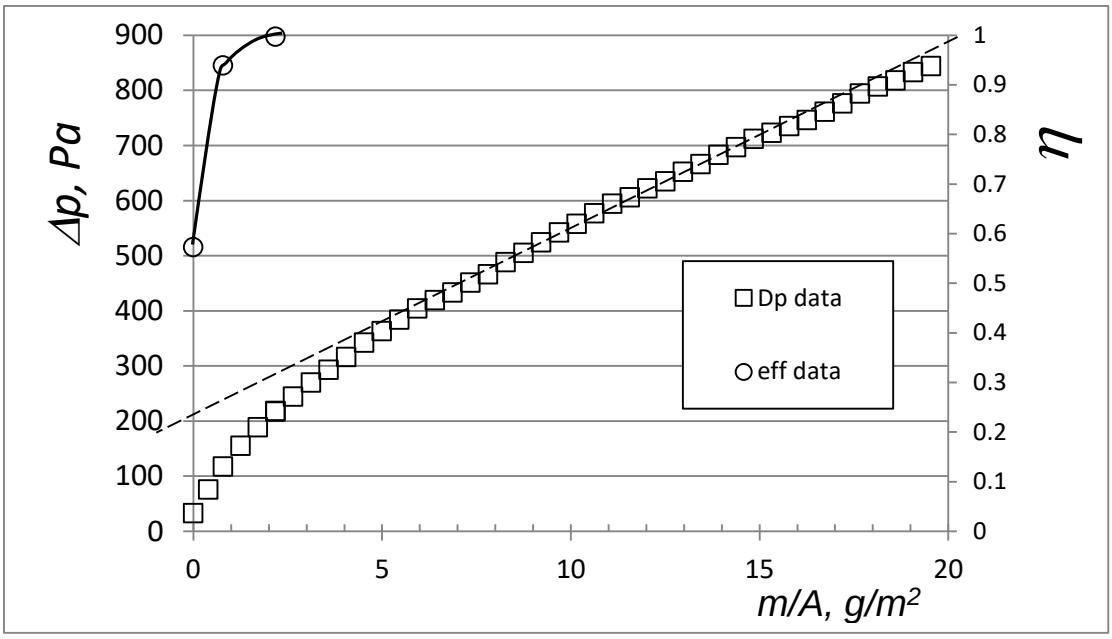

Fig. 6 – Loading curve for 187nm fiber diameter nanofiber filter. The slope of the cake regime (dotted line) is 35.75±0.75Pa/gm^{-2}.

4.2 Nanofiber filter (mean diameter 283nm)

The SEM image of the test filter with 283nm mean diameter is shown in Fig. 5b. Fig. 7 reveals the measured pressure excursion versus aerosol loading using a 283nm-diameter nanofiber filter. The overall behavior is somewhat similar to that of Fig. 6 for the 187nm-diameter nanofiber filter. The initial pressure drop was 28.5Pa. The pressure drop Δp rose under a longer time period exhibiting a concave downward behavior over increasing specific mass deposit m/A until reaching a steady linear increase rate. It is noted as m/A > 7 gm^{-2}, a cake was formed on the nanofiber filter surface capturing aerosols of all sizes. At 17.6 gm^{-2}, Δp reached the maximum pressure drop in the experiment of 850Pa and testing was stopped. The slope of the pressure excursion curve over aerosol loading in the cake filtration regime was determined to be 37.86(10^3) Pa-kg^{-1}m^2. Using Eqs. 3a, b and Eq. 6, the solids volume fraction, ε_s, was determined to be 0.0422 and the cake permeability, K, to be 2.73 (10^{-13})m^2, respectively. Again, these values

are comparable to that of 187nm diameter nanofiber filter. It appears that the increase in fiber diameter in the filter does not help in making a much more permeable cake above the filter. Despite the larger fiber diameter, the cake formed from the 283nm-diameter nanofiber filter still retained very high flow resistance, low porosity and permeability which were comparable to the cake formed on the 187nm diameter nanofiber filter.

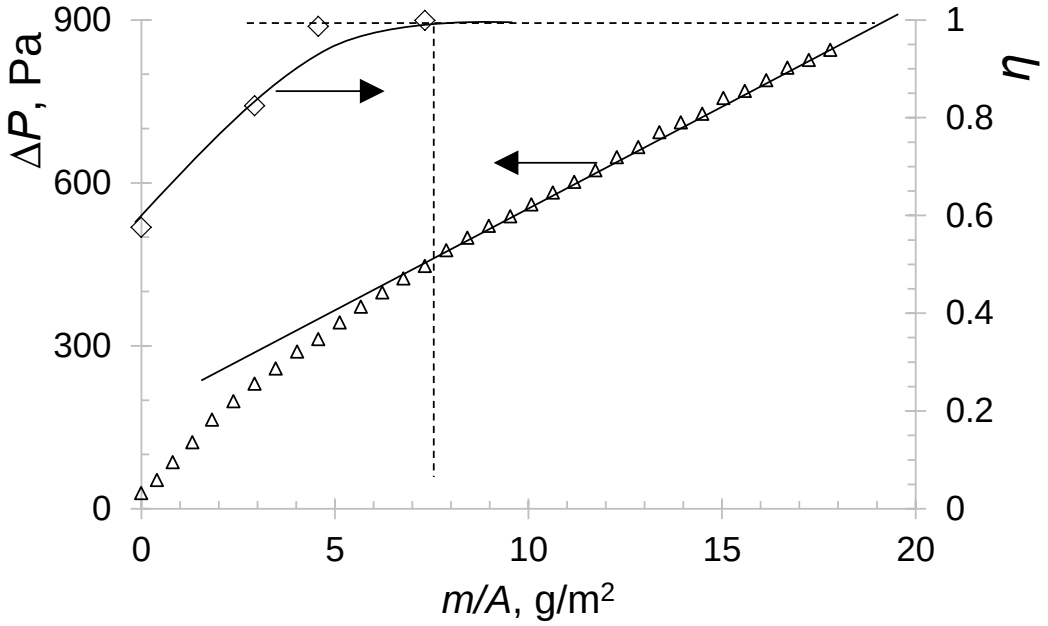

Fig. 7 – Loading curve for 283nm diameter nanofiber filter. The slope of the cake regime (solid line) is 39.09±0.63 Pa/gm^{-2}.

The low permeability for the nanofiber filters 2.73(10^{-13})m^2 and 2.57(10^{-13})m^2, respectively, for the 283-nm and 187-nm diameter nanofiber filter lead to high pressure drop during aerosol loading, which is a serious disadvantage for nanofiber filters. On the other hand, the advantage of the nanofiber filter is that the capture efficiency for nano-aerosols is quite high. Prior to investigating into possible improvement on nanofiber filter, let us examine the pressure drop behavior of microfiber filter subject to the same challenging aerosol loading.

4.3 Microfiber filter

Fig. 8 shows the loading curve test results of a microfiber filter with 2.7-micron fiber diameter. The initial filtration efficiency was less than 60% for specific aerosol loading below 4 gm^{-2} and it was as low as 40+% at the clean pristine state. Only until the specific aerosol loading has been doubled to 8gm^{-2}, the efficiency rose to 90%. The challenging aerosols were fully captured, i.e. 100%-efficiency, when the specific aerosol deposit *m/A* attained 18 gm^{-2} at which a cake formed on the surface of the microfiber filter. The initial pressure drop was 20.6Pa, which was smaller than those of the two nanofiber filters. The pressure drop Δp rose initially with a concave upward behavior (in contrast to the concave downward behavior for the two nanofiber filters) over increasing specific mass deposit *m/A* until reaching a steady linear increase. After depositing 20 gm^{-2}, the pressure drop across the microfiber filter reached 500 Pa, which was nearly half the pressure drop (about 900 Pa) when compared to those of the nanofiber filters. Indeed, from Fig. 8 the slope of the pressure excursion curve over aerosol loading in the cake filtration regime was only 27.70(10^3) Pa-$kg^{-1}m^2$. Based on this, the solids volume fraction, ε_s, from Eq. 3a was determined to be 0.0349, which was much less than that for the nanofiber filter, 0.0422-0.0475. Again, the cake permeability, *K*, was determined from Eq. 6 to be 4.50(10^{-13})m^2 which was 75% and 65% larger than the permeability for the two nanofiber filters, 2.57(10^{-13})m^2 – 2.73(10^{-13})m^2, respectively. This is largely by virtue of Eq. 6 given $K \sim 1/\varepsilon_s^2$ for small ε_s.

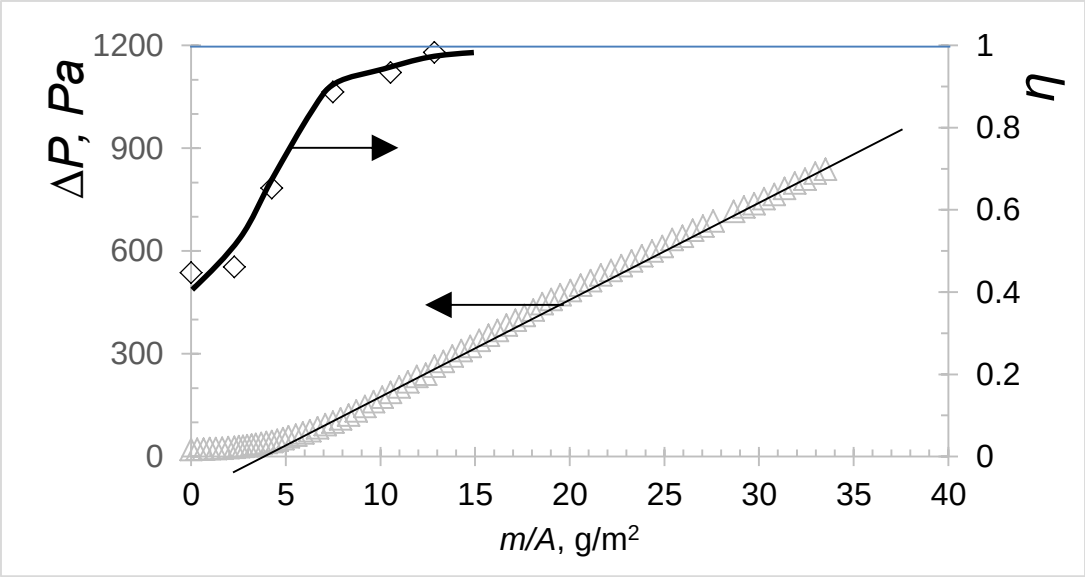

Fig. 8 – Loading curve for microfiber filter with 2.7-micron fibers. The slope of the cake regime (solid line) is 27.70±0.43 Pa/gm^{-2}.

If microfiber can provide more sites for dendrites to form on the fiber surfaces and these growing dendrites further interact to form a highly porous and permeable region around the fiber. The cake that forms on the microfiber filter would also be more permeable and porous. Would it be possible to realize the benefit of installing a microfiber filter upstream of the nanofiber filter (i.e. composite filter) so that the cake formed above the filter surface corresponds to the porous, permeable cake formed on the microfiber filter? Simultaneously, during initial filtration the nanofiber filter downstream in the composite filter provides a high efficiency for the composite filter covering the shortcoming of the microfiber filter. This is the basis of the composite filter technology conceived and developed [16].

Noted that both Fig. 6 and Fig. 7 for the two nanofiber filters exhibit the concave downward behavior for the pressure drop excursion over loading representing the higher-efficiency, high-skin effect [20] during initial filtration. In contrast, Fig. 8 for the microfiber filter exhibits a concave upward behavior for the pressure drop excursion over loading representing the lower-efficiency, low-skin effect [14] during

initial filtration. These two shapes can also be interchanged, such as from low skin behavior to high skin behavior during repeated loading-and-cleaning [21], whereby the loading curve changes from concave upward from the first loading cycle to concave downward from the second and higher cycles.

4.4 Microfiber-nanofiber composite filter

A composite filter with the microfiber (2.7-μm diameter) upstream and immediately the nanofiber (187-nm diameter) downstream was assembled for testing, see Fig. 3b. The results of the test are summarized in Fig. 9a. As shown, the microfiber-nanofiber composite filter has initial higher filtration efficiency 80-97% for $m/A< 5 gm^{-2}$ (versus 40-60% for microfiber filter for $m/A< 4 gm^{-2}$), and over 97% for $m/A>7\ gm^{-2}$. (Note if anything else, the efficiency of this composite filter should have been even higher and no less than that of the single nanofiber filter of 187nm as shown in Fig. 6. Essentially, both Fig. 6 and Fig. 9a should have close to 90-100% efficiency during initial loading.) This indeed demonstrates the advantage of including the nanofiber filter downstream of the composite filter to boost the capture efficiency prior to cake formation on the microfiber filter. As the mass deposit exceeds $12 gm^{-2}$, the capture efficiency for the 300nm reached 100%. At cake filtration regime, the pressure drop roses with increasing aerosol deposit with a linear increase rate of $26.63(10^3)$ Pa-$kg^{-1}m^2$ until reaching 610Pa at 20 gm^{-2}. The value of the slope for the composite filter was less than that of with the nanofiber filter alone, 35.75 (10^3) Pa-$kg^{-1}m^2$. Based on the slope of the pressure excursion curve for the composite filter, the cake ε_s was determined as 0.0279 and the cake permeability K as $5.87(10^{-13})m^2$. The cake solidosity 0.0279 was even less than that of the microfiber filter, 0.0349 while the cake permeability $5.87(10^{-13})m^2$ was higher than that of microfiber filter permeability $4.50(10^{-13})m^2$. The reduced solidosity in the cake might be related to the fact that there was lesser aerosols challenging the microfiber filter due to part of that being escaped downstream and got captured by the nanofiber filter. The dendritic structure which formed ultimately the cake on the microfiber filter was more loosely configured resulting in a more

porous and consequently permeable cake. At least it is conservative to remark that the cake is comparable to (and perhaps even better than that of) the microfiber filter. Indeed, the composite filter provides a more favorable filter as compared to a nanofiber filter in providing a cake with low solidosity, higher permeability and lower pressure drop. It is also more favorable as compared to the microfiber filter in that the initial efficiency is much higher than that of the microfiber filter alone, yet the pressure drop of the micro-nanofiber composite filter is only slightly higher than that of the microfiber filter in the initial period.

It is also instrumental to compare the pressure excursion curve between the composite filter with just the 187-nm nanofiber filter in Fig. 9b. The escalation of the pressure drop with a concave downward behavior of the single nanofiber filter is obvious. This is due to the high-skin effect of deposition of aerosols near the upstream end of the nanofiber filter [20]. On the other hand, by placing a microfiber filter immediately upstream of the nanofiber filter as with the composite filter, this concave increase in pressure drop is eliminated as shown in Fig. 9b. Further the cake is more permeable for the composite filter due to the microfiber filter while the nanofiber filter has a more tighter cake with lower permeability. This is reflected in the difference in slope of the pressure drop excursion curve in the cake region (linear portion of the curve). At $20 gm^{-2}$ of cake deposition, the pressure drop savings due to the use of composite filter is 30%. For larger aerosol deposition, this saving can be much substantial.

Next, we compare the composite filter with the microfiber filter in Fig. 9c. It is clear that the efficiency before 5-6 gm^{-2} of deposition is significantly higher, which is advantageous. At clean state, the efficiency for the composite filter is 80% while that of the microfiber filter is only 45%. The slope of the two cake lines are largely similar with the composite filter slightly less. At 40 gm^{-2} deposition, the pressure drop for the composite filter is 10% higher but this difference narrows down quickly with increasing aerosol loading. It is interesting to observe that the composite filter promotes the formation of the cake (attaining the linear trend) faster than that of the single microfiber filter. Once the cake forms, the cake

becomes the effective filter media as well as the storage for incoming aerosols. The cake can be removed during cleaning by backpulse and backblow more easily than when the aerosols are in the microfiber filter media. This is another subtle advantage of the composite media.

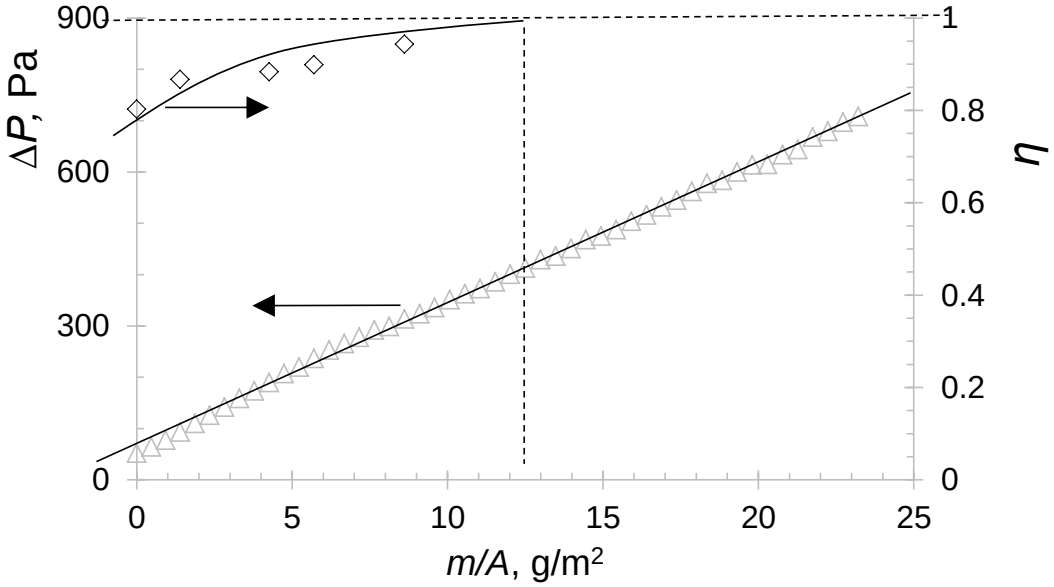

Fig. 9a – Loading curve for a microfiber (2.7-micron fiber diameter) upstream of a nanofiber filter (average fiber diameter 187nm) in a composite filter arrangement. The slope of the cake regime is 26.63±0.13Pa/gm^{-2}.

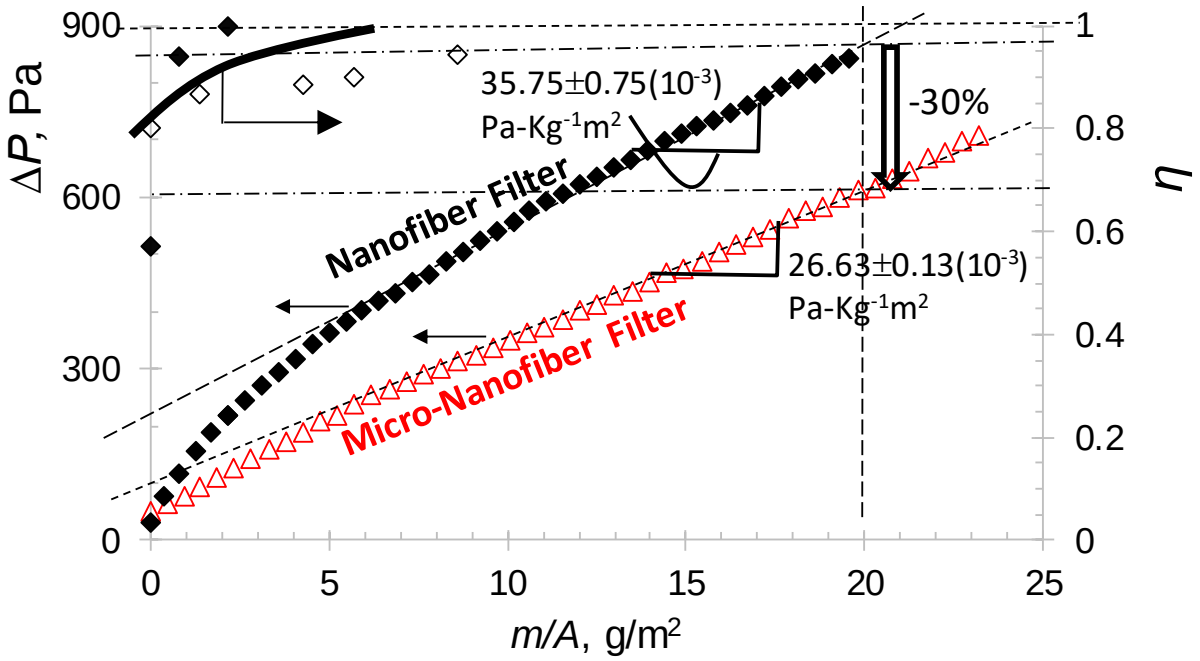

Fig. 9b – Comparing loading curve for a 2.7 micron microfiber-180nm nanofiber filter with single nanofiber filter.

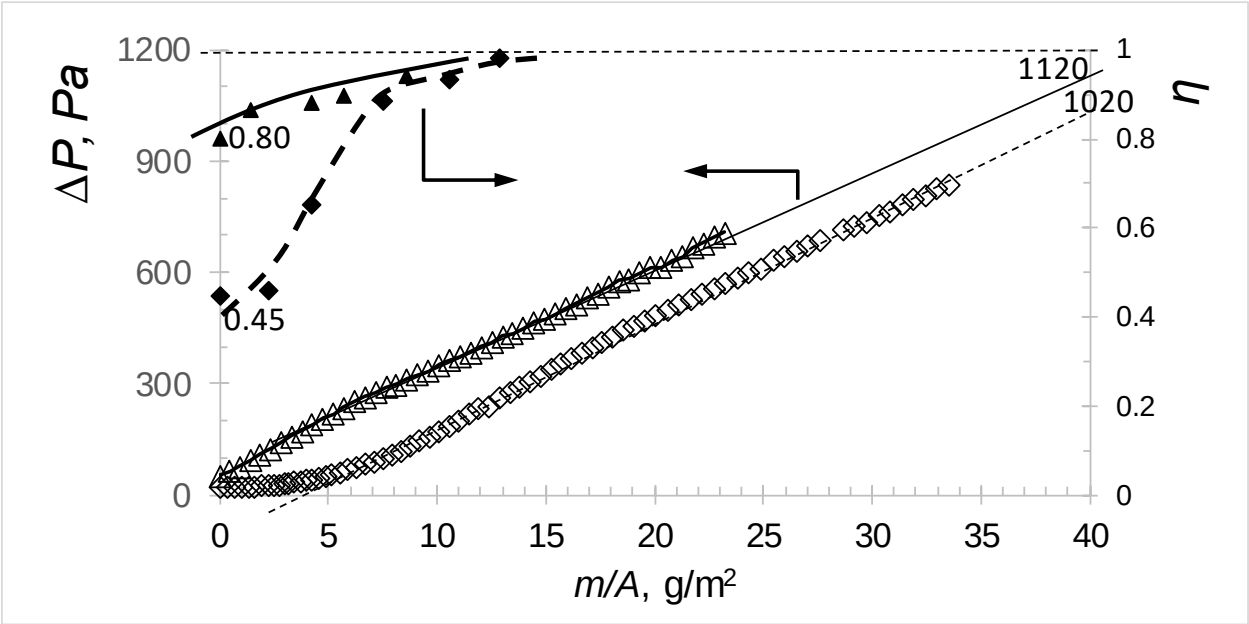

Fig. 9c – Comparing loading curve for a 2.7 micron microfiber-180nm nanofiber composite filter with single microfiber filter. Slope of microfiber cake line is 27.7±0.43Pa/gm^{-2} and the composite filter is 26.6±0.13Pa/gm^{-2}.

4.5 Microfiber filter (upstream) and nanofiber filter (downstream) separately installed

The filter combination is setup wherein a microfiber filter was positioned upstream in a test column and a nanofiber of 187nm is positioned much further downstream in the test column, see Fig. 3c. This configuration differs from the two filters being put together back-to-back as in section 4.4 (see Fig. 3b). In fact, as the nanofiber filter was located much further downstream of the test column, it had no influence on the microfiber filter upstream, therefore the microfiber filter acted independently whether the nanofiber was present downstream or not. The results of this setup are shown in Fig. 10.

The overall pressure drop across the two filters has a slight concave behavior with increasing specific mass deposit and reaches ultimately a linear behavior reflecting cake filtration. The microfiber filter started at pressure drop in a pristine state of 20.6Pa and it increased concave upward with increasing aerosol deposit until it reached a linear trend. The slope of the linear trend was 29(10^3) Pa-kg^{-1}m^2 which was the same as that of the overall pressure drop. This means that a cake was formed on the microfiber filter surface. This occurred when the overall efficiency reached say 95% at total mass deposit registered at 13 gm^{-2}. The nanofiber filter started at a pressure drop of 28.6Pa in pristine state and increased concave downwardly with increasing aerosol deposit until reaching a constant level at specific mass deposit of 13 gm^{-2} with no further change suggesting no challenging aerosols passed through from the microfiber filter to the downstream nanofiber filter. All incoming

aerosols were captured by the cake of the microfiber filter upstream. Also, a cake did not form on the surface of the nanofiber filter. It was obvious that beyond 13 gm^{-2} deposition, the nanofiber filter served no further filtration function in the combined filter setup in Fig. 3c. It is interesting the nanofiber filter played no role on the upstream microfiber filter. The efficiency shown in Fig. 10 refers only to the microfiber filter in the upstream. Essentially the microfiber filter in the combined filter acted as though it is a single microfiber in Fig. 8.

The overall pressure drop with aerosol deposit is compared between the microfiber-nanofiber separated filter with the microfiber-nanofiber composite filter in Fig. 11. The two filter configurations would have comparable efficiency. However, the pressure drop per increase in aerosol deposit in the cake regime for the microfiber-nanofiber composite filter was $26.63\pm0.13(10^3)$ Pa-$kg^{-1}m^2$). This was 7% lower when compared to the microfiber-nanofiber separated filter which was at $28.6\pm0.2(10^3)$ Pa-$kg^{-1}m^2$. This is evident in Fig. 10 based on the slope of the linear trend (cake filtration) in respective filter configuration. For the separated filter arrangement, the cake ultimately formed on the microfiber filter surface was independent of the nanofiber filter downstream. For the combined filter arrangement, there might be some possible interactions with the microfibers and their deposit from the cake layer of the nanofiber layer when it grew into the microfiber layer. This requires detailed study in the future using tomography or other in-situ techniques on mapping the cake structure and its growth over aerosol loading. Nonetheless, it is safe to say that the pressure drop per unit increase in cake deposition is not higher than that of the separated arrangement. This demonstrates the compact microfiber-nanofiber composite filter provides low pressure drop and high efficiency for filtration from start to end. The lower pressure drop means also lower power consumption as power is a product of flow rate and the pressure drop. This also means longer operation before filter replacement or cleaning as well. The other advantages of the microfiber filter in the composite arrangement is that it serves as a

prefilter in removing larger aerosols preventing clogging of the nanofiber filter by these larger aerosols. This advantage is applicable for both filter configurations. In summary, the microfiber-nanofiber composite filter offers a lower pressure drop as compared to the case where they are being separated. The microfiber filter also plays as the prefilter role in removing both large and small aerosols prior to the downstream nanofiber filter.

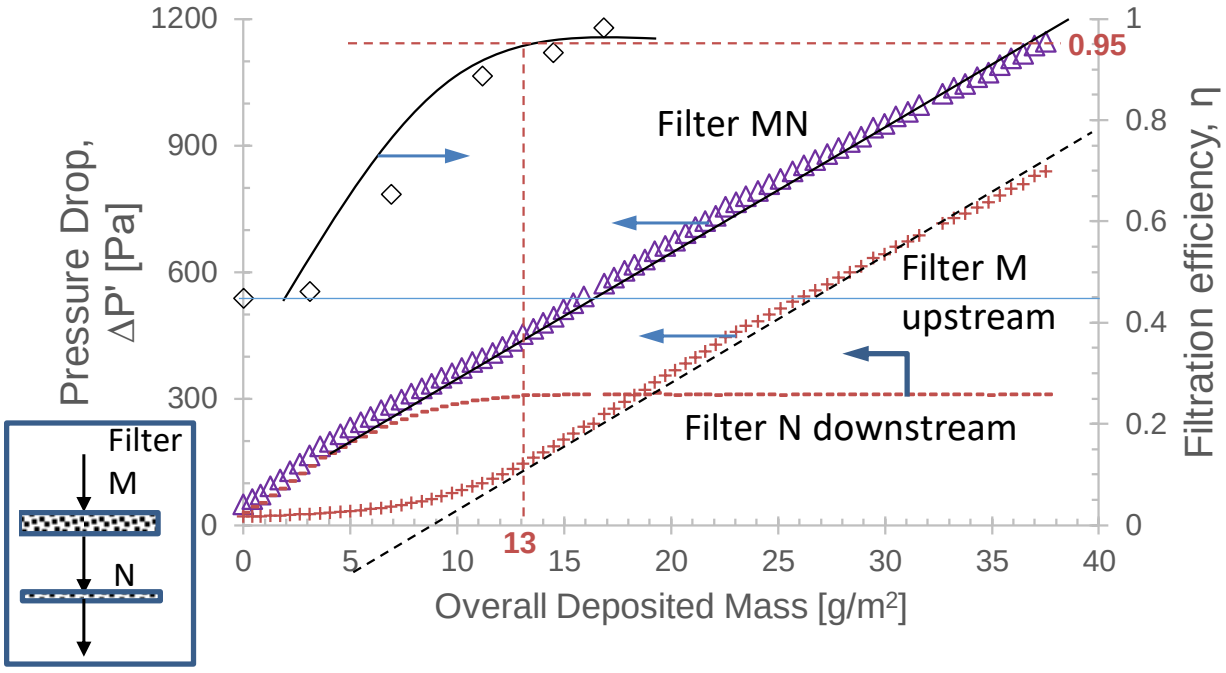

Fig. 10 – Microfiber (M) and nanofiber (N) filters are at different locations along the test column. They are being spaced apart.

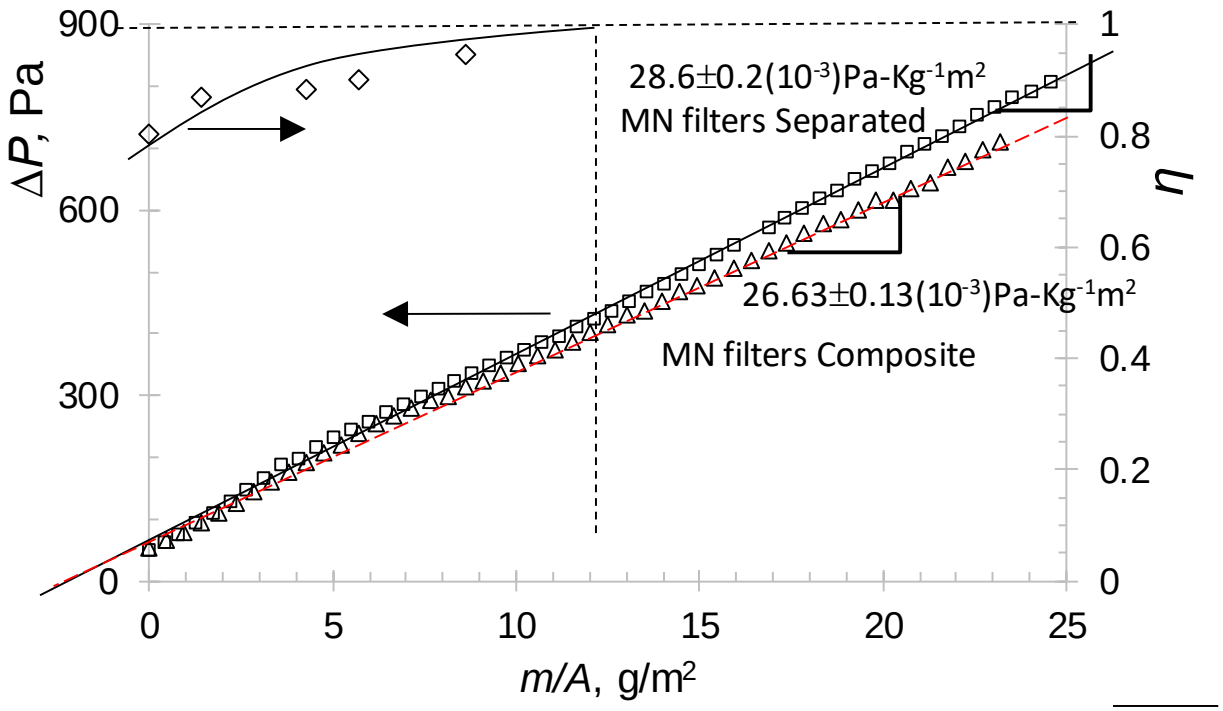

Fig. 11 – Comparing the microfiber-nanofiber separated filter with the microfiber-nanofiber composite filter.

4.6 Nanofiber-nanofiber composite filter

Contrary to a microfiber-nanofiber composite filter, we examine next a more permeable nanofiber filter with 283nm fiber diameter followed by 187nm fiber diameter nanofiber filter. The test results are shown in Fig. 12. As shown in the figure, the nanofiber-nanofiber dual filter has higher initial filtration efficiency of over 90% for $m/A < 3.5$ gm^{-2}. As the mass deposit exceeded 5 gm^{-2}, the capture efficiency for the 300nm (presumably other aerosol sizes) reached 100%. The pressure drop rose with aerosol deposit at cake filtration regime at a rate of 39.09(10^3)Pa-kg^{-1}m^2. Based on the slope of the pressure excursion curve, the cake ε_s was determined to be 0.0458 and the cake permeability K, 2.44(10^{-13})m^2. The cake solidosity was higher and the cake permeability was much lower than the all the filters being considered so far. This may be due to the cake formed from the 187nm nanofiber filter rose inside the 283nm layer without being rearranged to a more permeable,

porous structure. If anything else, the cake must have got more compacted with the high solidosity of 0.0458.

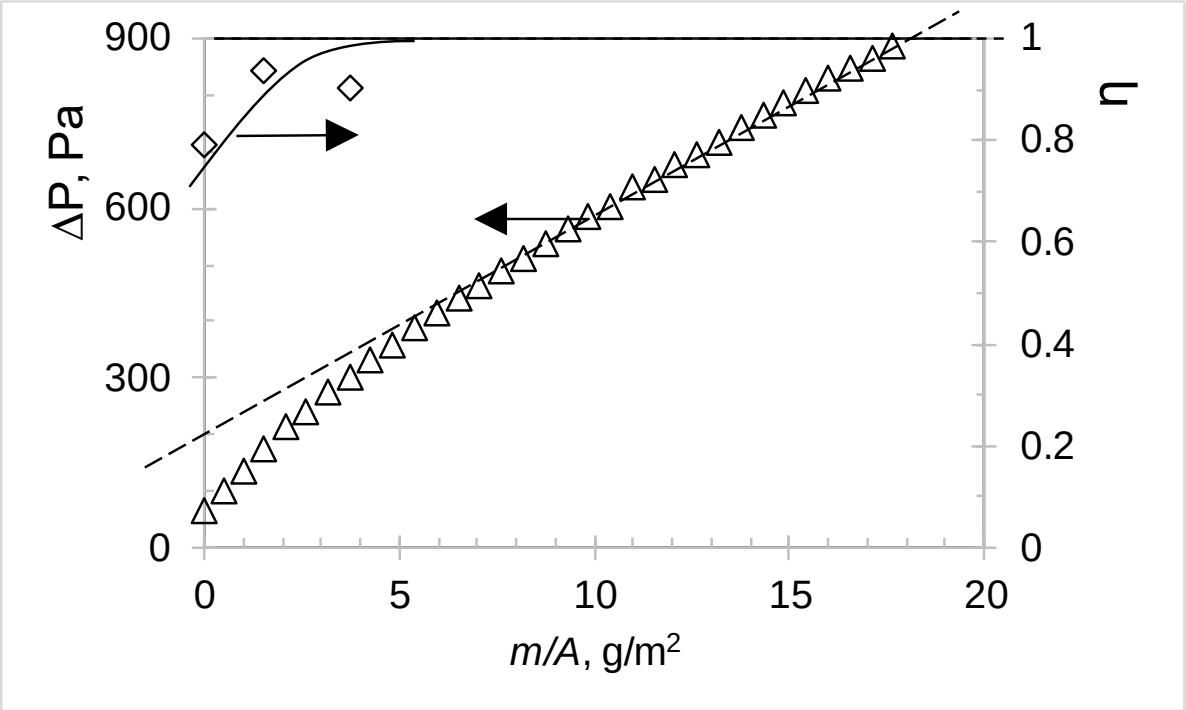

Fig. 12 – Loading curve for a nanofiber (287nm fiber diameter) upstream of another nanofiber filter (183nm fiber diameter). The slope of the cake regime (dotted line) is 39.09±0.63 Pa/gm^{-2}.

4.6 Cake from different filters

Table 2 compares the cake properties from the five different filters. These properties were inferred from combining the Ergun equation, slope of the pressure drop versus specific cake deposit plot, material balance, and Darcy's law as explained in Section 3. The first column lists the five different filters in the tests, second column the slope of the cake line, third column the dimensionless parameter to be explained in subsequent section, fourth column the solidosity of the cake, fifth column cake permeability, sixth column divided into two columns the ratio of the cake permeability of a given filter

to the 187nm diameter nanofiber cake, and microfiber filter cake, respectively, and the seventh column aerosol mean diameter in the challenging aerosol stream.

First the aerosol mean diameter is quite comparable among all five different tests and one can be assured that the test results are obtained from challenging different filters under the same aerosol diameter. Second, the solidosity of the cake from the two single nanofiber filters are comparable (0.0422 - 0.0475). By placing two nanofiber filters together with 283nm diameter upstream and 187nm diameter downstream, the cake solidosity is in between at 0.0458. A “compact” cake can still form with two layers of nanofiber filter installed as a composite filter. This may be due to the fact that the cake first forms on the surface of the 187nm filter. As the cake grows into the 283nm filter layer, it gets further compacted, if not loosened up. As the cake grows above the 283nm filter layer it retains its tight compact form with high solidosity. On the other hand, the cake solidosity of the microfiber filter is a lot lower at 0.0349 inferring the cake is much more porous and permeable. We certainly would prefer this form of the cake in the composite microfiber-nanofiber dual layer filter. Indeed, the last entry in column 2 of Table 2 reveals the solidosity of such composite filter is the least at 0.0279, or at least comparable to that of a single microfiber filter. The cake permeability, as determined in Eq. 6, is more or less behaves inversely with the cake solidosity. In the order of the highest to lowest, the composite microfiber-nanofiber filter, single microfiber filter, single layer nanofiber filter of 283nm, the composite 283nm-187nm dual layer nanofiber filter, and single layer nanofiber filter of 187nm. When the cake corresponding to the 187nm single layer nanofiber filter is used as a reference. The cake from the microfiber filter is 1.75 times more permeable, the composite micro-nanofiber filter is 2.29 times more permeable, whereas the cake corresponding to the 283nm-187nm dual layer nanofiber filter is 0.95 times more permeable.

On the other hand, when the cake corresponding to the microfiber filter is used as a reference, the cake from the composite micro-nanofiber filter is 1.3 times higher in permeability. One possible explanation

on this high permeability is due to that fact that during loading of the microfiber – nanofiber filter, some aerosols are captured by the upstream microfiber forming dendritic structure while most aerosols are passed to the downstream nanofiber filter with a large portion being captured and some being escaped. At some point, the growing dendritic structures interact that leads to cake formation in the microfiber filter. Similar phenomena also happened to the downstream nanofiber filter, but the cake from the microfiber filter forms first and grows above-and-beyond the surface of the composite filter faster than that from the nanofiber filter downstream. The cake is more porous and permeable as it springs off from the dendritic structures of the microfiber filter. On the other hand, the cake in the nanofiber filter provides a high capture efficiency for the composite filter during the initial filtration period prior to cake being formed in the microfiber layer.

Table 2 – Comparing the cake properties formed from the five different filters

Filter	Slope [Pa/gm^{-2}]	β [-]	Solids Volume Fraction, ε_s [-]	Permeability, K [m^2] x 10^{13}	Permeability Ratio		d_p* [nm]
Nanofiber filter 187nm diameter	35.75±0.75	2.185±0.046	0.0475±0.0008	2.57± 0.11	1	/	317
NN, 283nm-187nm Composite	39.09±0.63	2.276±0.037	0.0458±0.0006	2.44± 0.08	0.95	/	297
Nanofiber filter 283nm diameter	37.86±0.56	2.499±0.037	0.0422±0.0005	2.73± 0.08	1.06	/	288
Microfiber filter, 2.7	27.70±0.43	3.086±0.048	0.0349±0.0005	4.50± 0.14	1.75	1	303

micron diameter.							
Micro (2.7 micron)-Nano (187nm) Composite	26.63±0.13	3.955±0.019	0.0279±0.0001	5.87± 0.06	2.29	1.30	273

*mass mean diameter

4.7 – Dimensionless cake deposition-resistance ratio, β

4.7.1 Derivation and interpretation of cake deposition-resistance ratio, β

The solidosity and permeability are back-calculated from the value *C*, via Eq. 3b.

From Eq. 3b, we can define a dimensionless parameter β,

$$\beta = \left(\frac{3}{25}\right) C = \frac{18\mu V}{\rho_s d_p^2} \frac{1}{(\Delta p/\Delta m_s)} \quad (7)$$

In Appendix A, we have shown that β is proportional to the ratio of equivalent thickness of the cake solids (in a molten state) spread out on the filter area *A* (ΔL_s) to the equivalent flow resistance path/distance (ΔL_f) due to the additional cake deposition. It is “an inverse measure" of additional flow resistance (assuming viscous drag due to small Reynolds number flow) from addition cake deposit.

$$\beta = 18 \frac{\Delta L_s}{\Delta L_f} \quad (8)$$

Both ΔL_s and ΔL_f are defined below:

$$\Delta L_s = \Delta m/\rho_s A \quad (9a)$$

$$\Delta L_f = \Delta p d_p^2/(\mu V) \quad (9b)$$

ΔL_s represents the additional height of the cake deposit if it is all in "molten form" as in fluid and packed with uniform height/thickness on the filter surface with area, A. Note ΔL_s is related to the additional physical cake height by the solidosity factor, i.e. $\Delta L_s/\varepsilon_s$. ΔL_s is a kinematic parameter without dynamics. It represents the amount of cake deposition. On the other hand, ΔL_f represents the "equivalent drag distance" due to viscous flow through the additional cake deposit. It is a dynamic parameter. In Appendix A, we have also used Buckingham-π analysis to independently derive this ratio $\Delta L_s/\Delta L_f$ which has been demonstrated to be proportional to β. There, we have further developed the relationship ε_s=f(β) in details using Buckingham-π analysis.

4.7.2 Comparing cake deposition-resistance ratio, β, with conventional specific cake resistance, α

Here, we compare the cake deposition-resistance ratio to any possible existing parameter in the literature on filtration. From Eq. 7a, the incremental pressure drop across an additional deposition of cake per unit filter area m_s, is

$$\Delta p = \left(\frac{18\mu V}{\rho_s d_p^2}\frac{1}{\beta}\right)\Delta m_s \qquad (10)$$

In the literature, a dimensional average specific cake resistance, α_{av}, is used to measure the entire cake property with unit of mkg^{-1}. Using the incremental value of specific cake resistance α instead for the entire cake, we can also determine the incremental pressure drop across an additional deposition of cake per unit filter area m_s, as

$$\Delta p = \mu V \alpha \Delta m_s \qquad (11)$$

Comparing Eqs. 10 and 11, we obtain

$$\beta = \frac{18}{\rho_s d_p^2}\frac{1}{\alpha} \quad (12)$$

The new cake deposition-resistance ratio is inversely related to (a) the specific cake resistance α, (b) the intrinsic cake solid (particle) density ρ_s, and (c) the second power of the average particles d_p that make up the cake. Specifically for the same α, a cake made of smaller particles and/or smaller particle density would have much higher β than the cake with the same α yet with either large particles and/or higher particle density. Even though large α or small β reveals the cake resistance is high, β has considered the particle size and density as well, whereas the specific cake resistance α does not! Further, α is a dimensional quantity mkg^{-1}, whereas β is a dimensionless parameter, the inverse (i.e. $1/\beta$) of which measures the cake flow resistance to additional cake deposit, or the resistance length to the cake deposit height (in molten form). β is a more physical parameter to interpret than α, which has a dimension of length per unit mass.

4.7.3 Application of cake deposition-resistance ratio, β, to filter cake comparison

Large β is favorable as it represents more cake deposition with reduced flow resistance. Vice versa, small β is unfavorable as it represents less cake deposition with increased flow resistance

By arranging the filter configuration, it may be possible to deposit the cake at lower driving force due to the cake being more porous (lower solidosity and higher porosity) and permeable (higher *K*), i.e. larger β. Figs. 13 and 14 plot the solidosity together with porosity and permeability, respectively, as function of

β for the five different test filters being considered. It is clear from Fig. 13 and Fig. 14 that large β results in lower solidosity, higher porosity, and higher permeability. We have also included the approximated analytical expression in these plots for comparison. In Fig. 13, ε_s is obtained by solving the cubic equation Eq. 3a, the solid curve is the approximated solution Eq. 4 together with Eq. 9 when ε_s <<1. Thus,

$$\varepsilon_S \approx \frac{1}{3+\frac{25}{3}\beta} \tag{13}$$

It is clear that the composite filter has the highest β of nearly 4 and the least ε_s of approximately 0.0279, followed by the single microfiber filter β=3.086 with ε_s of 0.0349, the two single nanofiber filters with β *of* 2.185-2.499 and ε_s of 0.0475-0.0422, and lastly the nanofiber-nanofiber filter with values β *of* 2.276 and ε_s of 0.0458, which are in between the two single nanofibers. The permeability in Fig. 14 is determined from Eq. 6 with known ε_s and the mass mean diameter d_p obtained from Table 2. An approximate expression is obtained by assuming C=(25/3) β >>1, such that from Eq. 6,

$$K \approx \frac{25}{54} d_p^2 \beta^2 \tag{14}$$

The microfiber-nanofiber composite filter has the highest permeability of 5.87(10^{-13})m^2, this is followed by the single microfiber filter of 4.50(10^{-13})m^2, two single nanofiber filters of 2.57(10^{-13}) to 2.73(10^{-13})m^2, m^2, and least the nanofiber-nanofiber composite filter of 2.44(10^{-13})m^2. All the deviations representing uncertainties of the slope of the cake line, β, ε, and K are given in Table 2.

Both Figs. 13 and 14 reveal that the larger is β the more porous (small solidosity) and permeable (large permeability) is the cake. Thus, it is clear that the addition of the microfiber filter upstream of the nanofiber filter provides a more permeable cake that alleviates the pressure drop during aerosol loading especially under caking condition for which the filter spent most of the time. The permeability is even better than just with the microfiber filter alone.

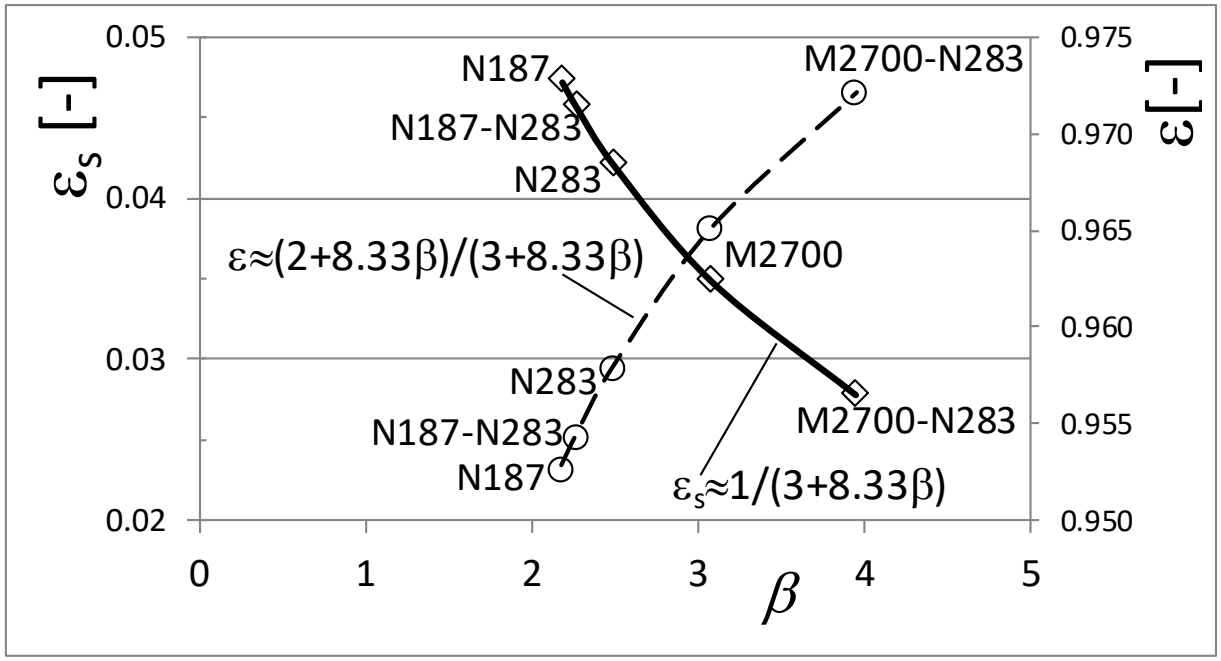

Fig. 13 – Comparing the solidosity and porosity of the cake for the five filters as a function of β.

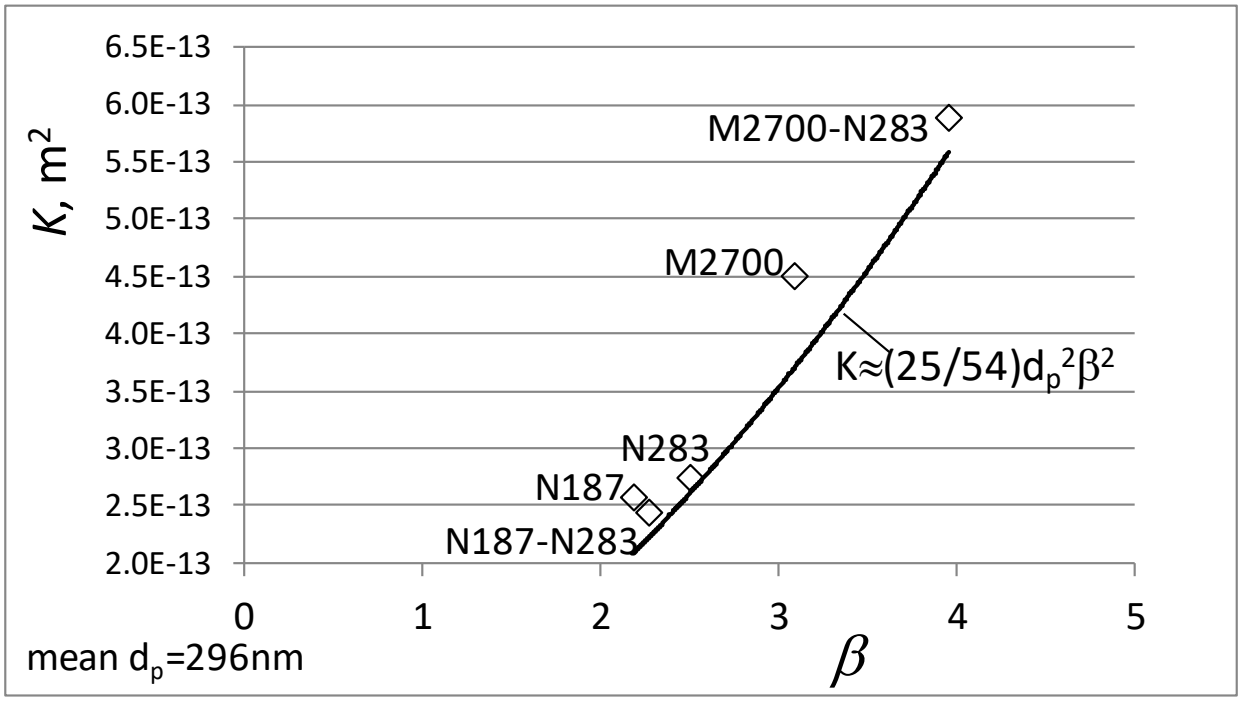

Fig. 14 – Comparing the permeability of the cake for the five filters as a function of β.

4.8 Cake deposition

For a nanofiber filter, once cake starts to deposit on the filter surface the cake properties, namely the porosity and permeability, can be determined. A rather impermeable cake results from the two single nanofiber filter with fiber diameter 187 and 283nm with the low permeability 2.57(10^{-13}) to 2.73(10^{-13})m^2. The cake can be perceived as shown in Fig. 15a. (This schematic perception is supported by CFD simulation to be presented in a separate publication.) With a composite nanofiber-nanofiber filter with tighter flowable pore size, the permeability is not much better, 2.44(10^{-13})m^2. On the other hand, a more porous microfiber filter with fiber diameter of 2.7μm yields cake permeability of 4.50(10^{-13})m^2, which nearly doubles that of the nanofiber filter. This is represented schematically by Fig. 15b (supported by CFD to be presented elsewhere). An intriguing issue is when a microfiber is placed immediately upstream of the nanofiber filter, from separate CFD results two cake layers would form, respectively, on the surface of the microfiber layer as well as on the surface of the nanofiber layer (growing into the microfiber layer) both attributed to the "skin effect" [14, 17] from each layer. The cake from the nanofiber would be rearranged as the cake grows passed by the microfibers in the microfiber layer. If the cake due to that of the nanofiber persists to grow into the microfiber layer, the cake would have a permeability better than that of a single nanofiber layer alone as the cake would be "restructured and reorganized" by both the dendrites/dendritic structure deposited on the microfibers and the microfibers themselves. On the other hand, the cake from the skin layer of the microfiber also grows as well, and if it grows sufficiently fast it can grow above the surface of the microfiber layer cutting off further aerosols passing downstream to build up the cake in the nanofiber layer. Which scenario would ultimately take control depends on the cake properties in the composite filter. From the experimental results we found indeed the permeability of the cake on the microfiber-nanofiber composite 5.87(10^{-13}) m^2 is closely

related to that of the microfiber filter $4.50(10^{-13})m^2$and not related to that of the 187-nm diameter nanofiber filter of $2.57(10^{-13})m^2$. Thus, we conclude that the cake forms on the microfiber layer outpaces that from the nanofiber layer downstream, which is extremely advantageous! In other words, the microfiber-nanofiber composite filter yields a cake that is almost the same or better than the single microfiber filter. This is represented schematically by Fig. 15c (supported by CFD to be presented separately) which is quite remarkable.

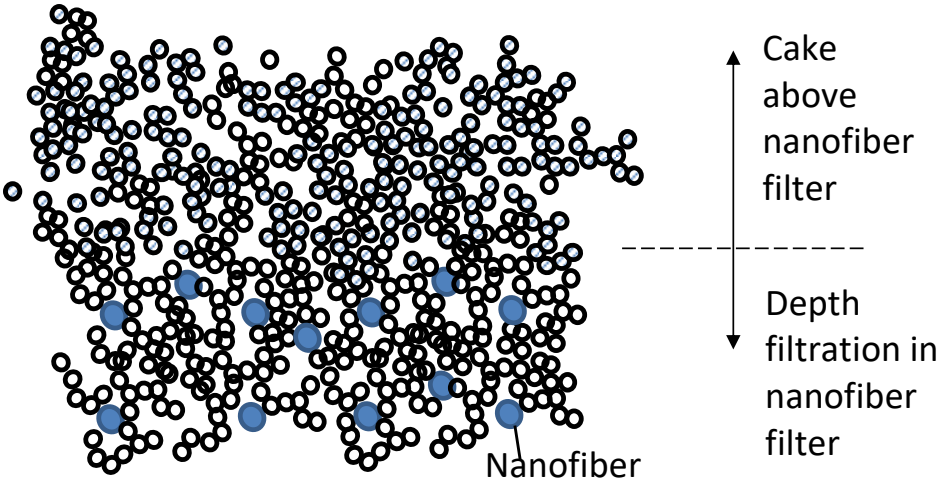

Fig. 15a – Nanofiber filter with trapped aerosols in the filter and in the cake layer formed. Aerosols are densely and randomly packed around nanofibers and above the cake. (schematic drawing)

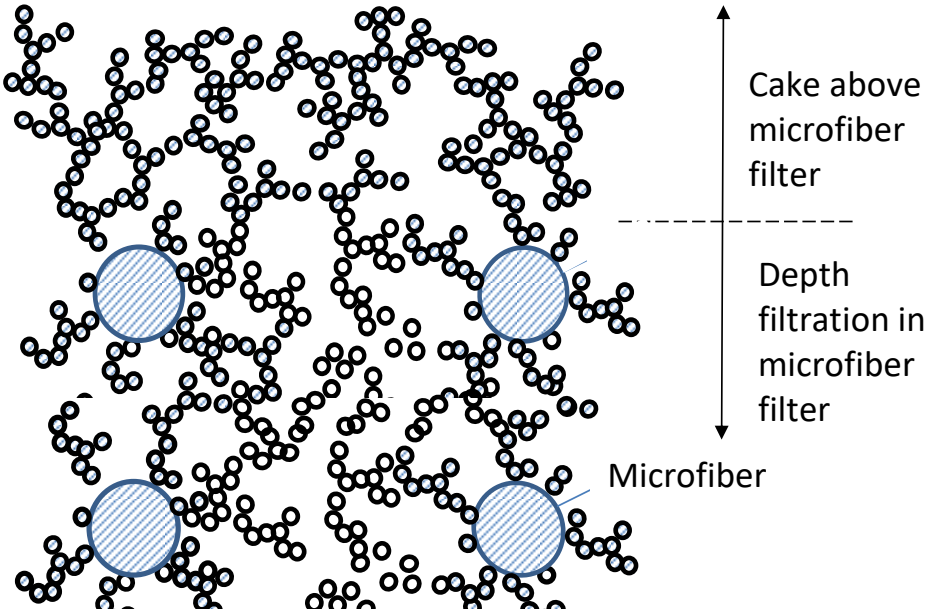

Fig. 15b – Microfiber filter with trapped aerosols in the filter and in the cake layer formed above the filter. Dendritic structures formed around the larger surface of the microfiber filter that help to space out the packing of aerosols. (schematic drawing)

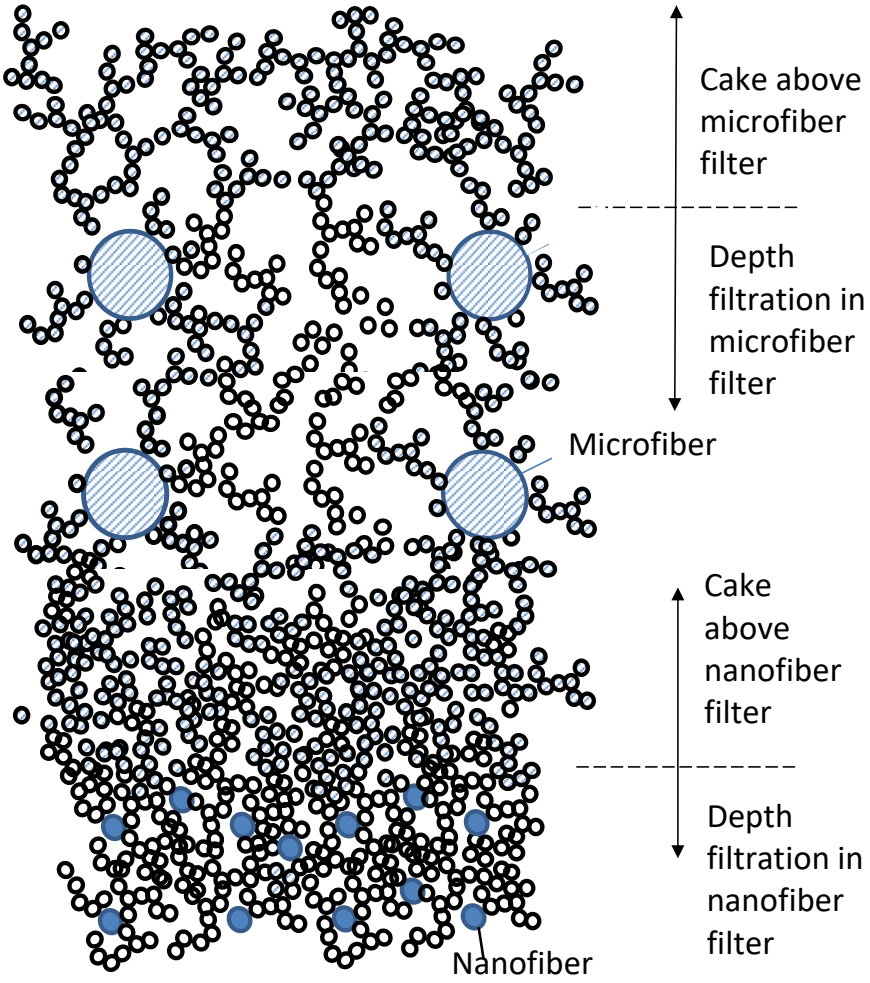

Fig. 15c – Nanofiber filter with packed aerosols. Above the nanofiber filter is a microfiber filter. Microfiber filter with trapped aerosols in the filter and in the cake layer formed above the filter. Dendritic structures formed around the larger surface of the microfiber filter help to space out the packing of aerosols. (schematic drawing)

5. Conclusions

Six different filter configurations with single nanofiber, single microfiber and combined microfiber-nanofiber, and combined nano-nanofiber filter have been tested. We are interested in the pressure drop during caking where filters operate mostly under such condition after initial period of depth filtration

followed by transition. An ideal filter for extended use is supposedly to have high efficiency, low pressure drop and high capacity for aerosols storage. In addition, during loading the efficiency should not be suddenly reduced due to covering of the fibers by the deposited aerosols as with the electret filter media. For prolonged operation, such as cabin filters, the aerosols are all stored in the cake and not in the filter media itself. The high capacity for an ideal filter therefore translates to low pressure drop per specific aerosol deposition in the cake. We have developed based on experiments and analytical models (Ergun equation on pressure drop in porous media, Darcy's law, and mass conservation) an approach to infer the cake solidosity, porosity, and permeability. This can also be quantified by a cake deposition parameter β. This parameter measures the additional cake deposition thickness (molten cake) to the viscous flow resistance path/distance from the additional cake deposition. β has also been independently derived using the Buckingham-π analysis. The higher is β the more permeable is the resultant cake deposit and the least is the pressure drop per unit aerosol deposition to overcome viscous friction. The composite microfiber (2.7μm)-nanofiber (187nm) filter has the highest $\beta \approx 4$, microfiber filter 3.1, nanofiber filters 2.2-2.5, and nanofiber (283nm)-nanofiber(187nm) filter 2.3. The composite micro-nanofiber filter stands out as the best performer in terms of pressure drop coupled with very high capture efficiency from in the entire filtration.

Under large aerosol loading the cake forms on the micro-nano composite filter surface originates from the microfiber layer with high permeability and low solidosity. This is very favorable as most of the operation, the filter is in cake filtration. Given the low pressure drop per gram of aerosol deposition, this increases the capacity of the filter, duration of operation before reaching maximum pressure drop, and reduces the operating power as the latter is a product of pressure drop and flow rate. We have also demonstrated that the composite filter has high initial filtration efficiency between 80-100% during

initial operation before cake filtration. This is much higher compared to a single microfiber filter that has an initial filtration efficiency of 40+%.

Acknowledgements

The authors want to thank the Hong Kong Research Grant Council in supporting the project under General Research Fund (GRF) PolyU 518012.

Nomenclature

A filter area, [m^2]

C concentration, [#/m^3] and constant (Eq. 3b)

d particle size/diameter, [m]

K permeability, [m^2]

L cake thickness, distance, [m]

m mass, [kg]

p pressure, [Pa]

s slope, [Pa/gm^{-2}]

t time, [s]

u face velocity, [ms^{-1}]

v volume, [m^3]

V face velocity, [ms^{-1}]

Greek

α specific cake resistance, [mkg^{-1}]

β dimensionless parameter, [-], Eqs. 9a and 9b

Δ change

ρ density, [kgm^{-3}]

ε volume fraction, [-]

η capture efficiency, [-]

μ viscosity, [$kg.m^{-1}s^{-1}$]

Subscript

c cake

d downstream

f filter, flow

i incipient to bridging

o before aerosol loading, i.e. m=0

p particle

s cake, solid, skin

u upstream

References

(1) W.W.F. Leung, C.H. Hung, and P.T. Yuan, Effect of face velocity, nanofiber packing density and thickness on filtration performance of filters with nanofibers coated on a substrate, Separation and Purification Technology, 71, 30-37, 2010.

(2) R.C. Brown. (1993). *Air Filtration: An Integrated Approach to the Theory and Applications of Fibrous Filters.* Oxford: Pergamon Press., 1993.

(3) C. Kanaoka, H. Emi, Y. Otani, T. Iiyama, Effect of charging state of particles on electret filtration, Aerosol Sci. and Tech., 7, 1-13, 1987.

(4) F. J. Romay , B. Y. H. Liu & S.-J. Chae, Experimental Study of Electrostatic Capture Mechanisms in Commercial Electret Filters, Aerosol Science and Technology, 28:3, 224-234, 1998.

(5) W. E. Teo, S. Ramakrishna, A review on electrospinning design and nanofibre assemblies. *Nanotechnology* 2006, *17* (14), R89-R106, DOI: 10.1088/0957-4484/17/14/R01.

(6) J. H. Wendorff, S. Agarwal, A. Greiner, Electrospinning: Materials, Processing, and Applications, Wiley-VCH: Weinheim, 2012.

(7) A. Greiner, J.H. Wendorff, Electrospinning: A Fascinating Method for the Preparation of Ultrathin Fibers. *Angew. Chem. Int. Ed.* 2007, *46* (30), 5670-5703, DOI: 10.1002/anie.200604646.

(8) W.W.F. Leung, C.H. Hung, Multilayer Nanofiber Filter, US Patent 8,523,971, Sept 3, 2013

(9) Y. Si, J. Yu, X. Tang, J. Ge, B. Ding, Ultralight nanofibre-assembled cellular aerogels with superelasticity and multifunctionality. *Nat. Commun.* **2014,** *5*, 5802, DOI: 10.1038/ncomms6802.

(10) P. Li, C. Wang, Y. Zhang, F. Wei, Air Filtration in the Free Molecular Flow Regime: A Review of High-Efficiency Particulate Air Filters Based on Carbon Nanotubes. *Small* 2014, *10* (22), 4543-4561, DOI: 10.1002/smll.201401553.

(11) S. Zhang, H. Liu, X. Yin, J. Yu, B. Ding, Anti-deformed Polyacrylonitrile/Polysulfone Composite Membrane with Binary Structures for Effective Air Filtration. *ACS Appl. Mater. Interfaces* 2016, *8* (12), 8086-8095, DOI: 10.1021/acsami.6b00359.

(12) N. Wang, Y. Yang, S.S. Al-Deyab, M. El-Newehy, J. Yu, B. Ding, Ultra-light 3D nanofibre-nets binary structured nylon 6–polyacrylonitrile membranes for efficient filtration of fine particulate matter. *J. Mater. Chem. A* 2015, *3*, 23946-23954, DOI: 10.1039/C5TA06543G.

(13) N. Wang, Y. Si, N. Wang, , G. Sun, M. El-Newehy, S.S. Al-Deyab, B. Ding, Multilevel structured polyacrylonitrile/silica nanofibrous membranes for high-performance air filtration. *Sep. Purif. Technol.* 2014, *126*, 44-51, DOI: 10.1016/j.seppur.2014.02.017.

(14) WWF Leung, HF Choy, "Transition from depth to surface filtration for a low-skin effect filter subject to continuous loading of nano-aerosols", Sep & Puri Tech, 190, 202-210, 2018.

(15) D. Thomas, F. X. Ouf, F. Gensdarmes, S. Bourrous, L. Bouilloux. Pressure drop model for nanostructured deposits. *Separation and Purification Technology*. 138, 144-152, 2014

(16) D. Thomas, P. Contal, V. Renaudin, P. Penicot, D. Leclerc, J. Vendel, Modelling pressure drop in HEPA filters during dynamic filtration, J. Aerosol Sci., Vol 30., #2, 235-246, 1999.

(17) W.W.F. Leung, C.H. Hung, Skin effect in nanofiber filtration of submicron aerosols, Separation and Purification Technology, 92, 174-180, 2012.

(18) W.W.F. Leung, C.H. Hung, and P.T. Yuan, Continuous filtration of sub-micron aerosols by filter composed of multi-layers including a nano-fiber layer, J. Aerosol Science and Technology, 43:1174–1183, 2009.

(19) W.W.F. Leung, Nanofiber Filter Facemask and Cabin Filter, United States patent 8,303,693, Nov 12, 2012

(20) WWF Leung, HF Choy, "Transition from depth-to-surface filtration for a high-efficiency, high-skin effect filter subject to continuous loading of nano-aerosols", Chem. Eng. Sci., 182: 67-76, 2018.

(21)W.W.F. Leung, WY Hau, Skin layer in cyclic loading-cleaning of a nanofiber filter in filtering nano-aerosols, Sep & Puri Tech, 188, 367-378, 2017.

Appendix A – Independent derivation and Interpretation of β

Recall β is defined as,

$$\beta = \frac{3}{25}C = \frac{18\mu V}{\rho_s d_p^2}\frac{1}{\left(\frac{\Delta p}{\Delta m_s}\right)} = 18\frac{\Delta m/\rho_s A}{\Delta p d_p^2/(\mu V)} = 18\frac{\Delta L_s}{\Delta L_f} \quad \text{(A1)}$$

$$\Delta L_s = \Delta m/\rho_s A \quad \text{(A2)}$$

Note ΔL_s represents the additional height of the cake deposit if it is all "melted" and placed on the filter with area, A. Note it is related to the additional physical cake height by the solidosity factor, i.e. $\Delta L_s/\varepsilon_s$. ΔL_s is a kinematic parameter. On the other hand,

$$\Delta L_f = \Delta p d_p^2/(\mu V) \quad \text{(A3)}$$

Note ΔL_f represents the "equivalent drag distance" due to viscous fluid (in this case air) flowing through the additional cake deposit. It is a dynamic quantity. β (or for that matter C) is actually a ratio of the kinematic cake deposition height (assuming all solids are melted with 100% solidosity) to the dynamic drag distance from viscous airflow through the additional cake deposition. Large β refers to cake deposition with little flow resistance; vice versa small β refers to large flow resistance with small cake deposition. Obviously, this all depends on how the aerosols or particles in the cake are being packed and

arranged. Logically, having small flow resistance means the solidosity should be small and the cake is highly porous; and vice versa. In other words, β and ε_s are related. We can write

$$\varepsilon_s = f(\beta) \quad \text{(A4)}$$

$$\beta = f^{-1}(\varepsilon_s) \quad \text{(A5)}$$

Indeed, the inverse function f^{-1} is given by Eq. 3a with β=(3/25)C.

Interestingly, β can also be found from a rigorous Buckingham-π analysis as follows. The following 10 governing variables to the problem are, respectively, fluid viscosity μ, face velocity u, solids volume v_s, cake volume v_c, filter area A, aerosol/particle density ρ_s, fluid density ρ_f,aerosol equivalent diameter d_p, additional pressure drop for new cake deposit Δp, and additional cake deposit Δm. The basic fundamental dimensions are length [L], [M], and [T]. According to the Buckingham-π analysis, we will get 7 (=10-3) dimensionless π groups. We have selected accordingly 3 fundamental variables μ, u, and ρ_f to form the π groups. Without the details of derivation, the results are given below:

$$\pi_1 = \frac{\mu}{\rho_f u d_p} \quad \text{(A6)}$$

$$\pi_2 = \frac{\Delta V_s}{{d_p}^3} \quad \text{(A7)}$$

$$\pi_3 = \frac{\Delta V_c}{{d_p}^3} \quad \text{(A8)}$$

$$\pi_4 = \frac{A}{{d_p}^2} \quad \text{(A9)}$$

$$\pi_5 = \frac{\rho_s}{\rho_f} \quad \text{(A10)}$$

$$\pi_6 = \frac{\Delta p}{\rho_f u^2} \quad \text{(A11)}$$

$$\pi_7 = \frac{\Delta m}{\rho_f {d_p}^3} \quad \text{(A12)}$$

These variables represent the inverse Reynolds number, dimensionless actual cake solid volume, dimensionless bulk cake volume, dimensionless filter area, density ratio of solid-to-fluid, dimensionless pressure drop, and dimensionless cake mass deposit. We are at liberty to form new π groups with the existing ones provided we still maintain 7 independent π groups. Consider, the ratio of π_2/π_3 which is the cake solidosity ε_s to replace π_2, then we will have the new list π_1 , π_8 , π_3, π_4 , π_5, π_6 , and π_7. We can write a general relationship as follows:

$$\varepsilon_s = \pi_8 = \pi_2/\pi_3 = fn(\pi_1, \pi_3, \pi_4, \pi_5, \pi_6, \pi_7) \qquad \text{(A13)}$$

Note not all π groups are important in determining the functional form of ε_s. Indeed, some may not be even important, such as π_3 and they will be dropped out. It can be shown that a new π_9 group can be formed such that

$$\pi_9 = \frac{\pi_1\pi_7}{\pi_4\pi_5\pi_6} = \frac{\left(\frac{\mu}{\rho_f u d_p}\right)\left(\frac{\Delta m}{\rho_f {d_p}^3}\right)}{\left(\frac{A}{{d_p}^2}\right)\left(\frac{\rho_s}{\rho_f}\right)\left(\frac{\Delta p}{\rho_f u^2}\right)} = \frac{\mu u}{\rho_s d_p^2}\frac{(\Delta m/A)}{\Delta p} = \frac{C}{150} = \frac{\beta}{18} \qquad \text{(A14)}$$

π_9 equals to $\beta/18$. Based on Eq. A1, π_9 is the ratio of the kinematic cake solids (melted) height to the flow resistance distance, $\Delta L_s / \Delta L_f$. This is rather remarkable that the Buckingham π analysis also bears out this important parameter!

One can express,

$$\varepsilon_s = \pi_8 = fn(\pi_9) = fn_2(\beta) \qquad \text{(A15)}$$

The rest of π groups are not important for determining ε_s.